Enclosure Effects on Flame Spread Over Solid Fuels in Microgravity‡

YUJI NAKAMURA,†,* TAKASHI KASHIWAGI, KEVIN B. MCGRATTAN, and HOWARD R. BAUM

Building and Fire Research Laboratory, National Institute of Standard and Technology, 100 Bureau Dr., Mail Stop 8663, Gaithersburg, MD 20899-8663 USA

Enclosure effects on the transition from a localized ignition to subsequent flame growth over a thermally thin solid fuel in microgravity are numerically investigated by solving the low Mach number time-dependent Navier-Stokes equations. The numerical model solves the two and three dimensional, time-dependent, convective/diffusive mass, and heat transport equations with a one-step global oxidation reaction in the gas phase coupled to a three-step global pyrolysis/oxidative reaction system in the solid phase. Cellulosic paper is used as the solid fuel and is placed in a slow imposed flow parallel to the surface. Ignition is initiated across the width of the sample or at a small circular area by an external thermal radiation source. Two cases are examined; an open configuration (i.e., without any enclosure) and the case with the test chamber used in our previous microgravity experiments. Numerical results show that the upstream centerline flame spread rate for the case with the enclosure is faster than that for the case without any enclosure. This is due to the confinement of the flow field and also thermal expansion initiated by heat and mass addition in the chamber. The confinement accelerates the flow in the chamber, which enhances oxygen transport into the flame. In the three-dimensional configuration with the spot ignition, the flame growth in the direction perpendicular to the flow is significantly enhanced by the confinement effects. The effect of the enclosure is most significant at the slowest flow condition investigated and the effect becomes less important with an increase in imposed flow velocity. The total heat release rate from the flame during a flame growth period increases significantly with the confinement and the enclosure effects should be accounted to avoid underestimating fire hazard in a spacecraft.

NOMENCLATURE

A	cross-sectional area at entrance of flow [cm^2]
B	frequency factor [1/s, 1/min]
C_p/C_v	specific heat of constant pressure/ volume [J/(g K)]
c_{pS}	specific heat in solid [J/(g K)]
D	diffusivity [cm^2/s]
E	activation energy [J mole]
h	enthalpy [J]
$\dot{I}$	external radiation [W/cm^2]
k	thermal conductivity [W/(cm K)]
M	molecular weight [g/mole]
$\dot{m}$	mass flux via decomposed reactions in solid [g/(cm^2 s)]
n	exponent of mass fraction in solid phase reactions
p	pressure [Pa]
Pr	Prandtl number
q	heat of combustion of evolved products [J/g]
r	surface reflectivity
R	universal gas constant, 8.314×10^{-3} [J/(K mole)] and radius of irradiation on sample [cm]
T	temperature [K]
t	time [s]
u	velocity vector [cm/s]
u	velocity component in each direction [cm/s]
u_w	imposed flow velocity [cm/s]
Vsp	upstream spread rate [cm/s]
x	x-direction [cm]
Y	mass fraction
y	y-direction [cm]
z	z-direction

Greek Symbols

δ	thickness of solid [cm]
ϵ	surface emissivity
γ	ratio of specific heats [$= c_p/c_v$], 1.4

*Corresponding author. E-mail: yuji@mech.nagoya-u.ac.up
†Guest Researcher, Present address: Department of Mechanical Engineering, Nagoya University, 1 Furo-cho, Chikusaku, Nagoya, Japan 464-8603.

COMBUSTION AND FLAME 130:307–321 (2002)

0010-2180/02/$–see front matter
PII S0010-2180(02)00381-4

ν	stoichiometric constant
ρ	density [g/cm^3]
σ	Stefan-Boltzman constant, 5.67×10^{-12} [W/(cm^2 K^4)]
τ	stress tensor
$\dot{\omega}$	reaction rate (gas-phase) [g/(cm^3 s)] (solid phase) [1/s]

Sub/superscripts

0	initial (ambient) state
A	ash
C	char
char	char oxidation reaction in solid phase reaction
F	virgin solid fuel (cellulose)
f	fuel gas (combustible gas component)
g	gas phase
i	i-th component
O2	oxygen involved term
ox	oxygen (in gas phase) oxidative degradation reaction in solid phase reaction
p	pyrolysis reaction of cellulose in solid phase reaction
rad	irradiation center
S	solid phase
thrm	thermal expansion
x	x-direction
y	y-direction
z	z-direction
*	relative value

INTRODUCTION

A number of studies on solid phase combustion in microgravity have been performed extensively in the past decade to assess the fire safety of spacecraft as well as to gain a better understanding the physical processes. Following Olson's experimental observations [1], theoretical models have been developed to understand flame spread in microgravity. Following the work of Frey and Tien [2], two-dimensional steady-state models [3, 4] were extensively developed and recently expanded into the three-dimensions (but still steady-state) [5]. Other models, including by those developed at NIST, were designed to capture time-dependent phenomena in both two [6–8] and three dimensions [9–11].

Despite these developments, very few calculations have taken into account the effects of an enclosure on flame spread. The effects of an enclosure could be important because the actual experiments conducted in microgravity were performed in a test chamber whose volume was rather limited. The expansion caused by the generation of heat and mass reaches the enclosure walls essentially instantaneously and modifies the flow field, potentially altering the flame growth behavior. Recently the behavior of the concurrent flame spread in a tunnel chamber was studied numerically by Shih and Tien [5, 12]. Their numerical model was based on 2-D [12] and 3-D [5] steady-state, elliptic formulations with finite-rate reactions in the gas and solid phases. It was found that the flame spread rate of narrow samples tends to be slower than those of wider samples because of heat loss from the flame to walls. However, when flame growth is controlled by oxygen supply to the flame, enhanced oxygen diffusion from the outer flow field near the walls to the flame increased the flame spread rate of the narrower samples. In addition, Baum and Kashiwagi [13] theoretically addressed the importance of the effect of an enclosure on heat transfer and burning of a solid fuel in microgravity in their 2-D steady-state, parabolic analysis.

These previous studies show clearly the importance of enclosure effects on combustion in microgravity. We are interested in determining such effects for our experiments, which have been designated the Radiative Ignition and Transition to Spread Investigation (RITSI), and have been performed in the Space Shuttle and in the drop tower at the Japan Microgravity Center, JAMIC. The test chamber is 85-mm wide, 95-mm high, and 171-mm long [14]. The differences between this study and those of Shih and Tien [5, 12] are twofold: the primary interest of this study is the effect of the RITSI enclosure on *time-dependent* flame growth phenomena from localized ignition instead of their steady-state flame growth, and the localized ignition is initiated at the center of the sample (mainly opposed flame growth) rather than concurrent flame growth. The objective of this work is to determine numerically the effects of the RITSI enclosure on the transition from localized ignition to flame spread in 2-D and

3-D configurations with the imposed flow velocity as a parameter.

An important consideration is the velocity boundary condition far from the flame. All previous theoretical studies except references by NIST researchers [7, 8, 10, 11, 15] assumed that the flow field at the boundaries of the computational domain did not change with the addition of heat and mass from the flame. As described above, the release of heat and mass generates an expansion field that affects the entire flow field. In our calculations to date, the inlet flow velocity was altered by the expansion field obtained from an analytical solution of a potential equation. With the enclosure, it is difficult to extend this approach to obtain the inlet flow condition. Two approximate flow field boundary conditions are used in this study to assess the importance of this problem.

MODEL DESCRIPTION

Solid Phase Model

A complete description of the theoretical model of the solid phase has been given in Refs. 7 and 10, and therefore, only a brief description is given here. The governing solid phase equations are:

$$\text{Mass}\quad \frac{\partial(\rho_S/\rho_{S0})}{\partial t} = -(1-\nu_{C,p})\dot{\omega}_p - (1-\nu_{C,ox})\dot{\omega}_{ox} - (1-\nu_{A,char})\dot{\omega}_{char}$$

$$\text{Energy}\quad \delta\rho_S c_S \frac{\partial T_S}{\partial t} = (q_p\dot{\omega}_p + q_{ox}\dot{\omega}_{ox} + q_{char}\dot{\omega}_{char})\rho_{S0}\delta + \nabla_{x,y}\cdot(k_S\nabla_{x,y}T_S)\delta + (1-r)\dot{I} - \epsilon\sigma(T_S^4 - T_0^4) + k_g\left.\frac{\partial T_g}{\partial z}\right|_{z=0}$$

Species [virgin paper (cellulose) and char]

$$\text{Cellulose:}\quad \frac{\partial(\rho_S Y_F/\rho_{S0})}{\partial t} = -\dot{\omega}_p - \dot{\omega}_{ox}$$

Char:

$$\frac{\partial(\rho_S Y_{char}/\rho_{S0})}{\partial t} = \nu_{C,p}\dot{\omega}_p + \nu_{C,ox}\dot{\omega}_{ox} - \dot{\omega}_{char}$$

Reaction rates

$$\text{Pyrolysis:}\quad \dot{\omega}_p = B_p\left(\frac{\rho_S}{\rho_{S0}}Y_F\right)^{n_{F,p}}\exp\left(-\frac{E_p}{RT_S}\right)$$

Paper oxidation:

$$\dot{\omega}_{ox} = B_{ox}(Y_{ox})^{n_{O2,ox}}\left(\frac{\rho_S}{\rho_{S0}}Y_F\right)^{n_{F,ox}}\exp\left(-\frac{E_{ox}}{RT_S}\right)$$

Char oxidation:

$$\dot{\omega}_{char} = B_{char}(Y_{ox})^{n_{O2,char}}\left(\frac{\rho_S}{\rho_{S0}}Y_C\right)^{n_{C,char}}\cdot\exp\left(-\frac{E_{char}}{RT_S}\right)$$

A thermally thin cellulosic paper is used as a solid fuel. Three exothermic degradation reactions are assumed for the pyrolysis of cellulose, thermal oxidation and char oxidation. The global reaction parameters and thermal properties of the solid sample are identical to those of past studies [10, 16]. Thermal conduction parallel to the sample and radiative energy loss from the surface are taken into account. Note that the specific heat and thermal conductivity of the sample paper are given as a linear function of temperature. More detailed discussion of the degradation of the paper can be found in Refs. [8, 16]. All properties of the sample paper used in the present study are summarized in Table 1.

Gas Phase Model

As for the gas phase, because the imposed flow velocity is very low (up to 10 cm/s), the low Mach number approximation and the perfect gas law assumption are applied. The test chamber opens to a large volume, thus, a constant background pressure is assumed. The governing gas phase equations are

$$\text{Mass}\quad \frac{\partial\rho_g}{\partial t} + \nabla\cdot(\rho_g\mathbf{u}) = 0$$

TABLE 1

Thermal-, Chemical-, Physical-Properties of the Sample Paper

Pyrolysis reaction parameter [10, 16]	
B_p: frequency factor; 1/s	3.0×10^{18}
E_p: activation energy; kJ/mole	237
$n_{F,p}$: exponent of Y_F	1.2
$\nu_{C,p}$: mass-based stoich. constant	0.14
$\nu_{f,p}$: mass-based stoich. constant	0.23
q_p: heat of combustion; J/g	64
Oxidative degradation reaction parameter [10, 16]	
B_{ox}: frequency factor; 1/s	5.0×10^{18}
E_{ox}: activation energy; kJ/mole	224
$n_{O2,ox}$: exponent of Y_{ox}	0.4
$n_{F,ox}$: exponent of Y_F	1.0
$\nu_{C,ox}$: mass-based stoich. constant	0.2
$\nu_{f,ox}$: mass-based stoich. constant	0.16
$\nu_{O2,ox}$: mass-based stoich. constant	0.41
q_{ox}: heat of combustion; J/g	1000
Char oxidation reaction parameter [10, 16]	
B_{char}: frequency factor; 1/s	1.0×10^{11}
E_{char}: activation energy; kJ/mole	166
$n_{O2,char}$: exponent of Y_{ox}	1.0
$n_{C,char}$: exponent of Y_C	1.0
$\nu_{A,char}$: mass-based stoich. constant	0.02
$\nu_{f,char}$: mass-based stoich. constant	0.52
$\nu_{O2,char}$: mass-based stoich. constant	1.65
q_{char}: heat of combustion; J/g	2400
Thermal- & physical properties [10]	
c_{pS}: specific heat of solid; J/(gK)	$0.96 + 4.19 \times$ (T-300)
k_S: thermal conductivity of solid; W/(cmK)	$3.55 + 1.55 \times 10^{-2} \times$ (T-300)
δ: thickness of solid; cm	0.013
ρ_S: surface density; g/cm^2	5.7×10^{-3}
ϵ: surface emissivity	0.6
r: surface reflectivity	0.25

$$\text{Momentum} \quad \rho_g\left(\frac{\partial \mathbf{u}}{\partial t} + (\mathbf{u}\cdot\nabla)\mathbf{u}\right) + \nabla p = \nabla\cdot\tau$$

$$\text{Energy} \quad \frac{\partial}{\partial t}(\rho_g h_g) + \nabla\cdot(\rho_g \mathbf{u} h_g) = q_g\dot{\omega}_g + \nabla\cdot k_g\nabla T_g + \nabla\cdot\sum_i h_{g,i}(\rho_g D)_i \nabla Y_{g,i}$$

$$\text{Species} \quad \frac{\partial}{\partial t}(\rho_g Y_{g,i}) + \nabla\cdot(\rho_g \mathbf{u} Y_{g,i}) = \nabla\cdot(\rho_g D)_i \nabla Y_{g,i} - \nu_{g,i}\dot{\omega}_g$$

$$\text{Equation of State} \quad p_0 = \rho_g T_g R \sum\left(\frac{Y_{g,i}}{M_i}\right) = \rho_g T_g R/M$$

Reaction Rate

$$\dot{\omega}_g = B_g \rho_g Y_{g,f} Y_{g,ox} \exp\left(-\frac{E_g}{RT_g}\right)$$

Three additional assumptions are made. First, the specific heats are assumed to be independent of temperature. Second, the Prandtl number (Pr) is assumed to be constant (0.7). Third, the radiative heat transfer from the flame to the sample surface is assumed to be negligible. This last assumption is based on the following ratio-

TABLE 2

The Gas Phase Reaction Parameters

Gas phase reaction parameter [10]	
B_g: frequency factor; 1/s	5.0×10^9
E_p: activation energy; kJ/mole	67
ν_g: mass-based stoich. constant	3.213 (modified from Ref. 10)
q_g: heat of combustion; J/g	35000

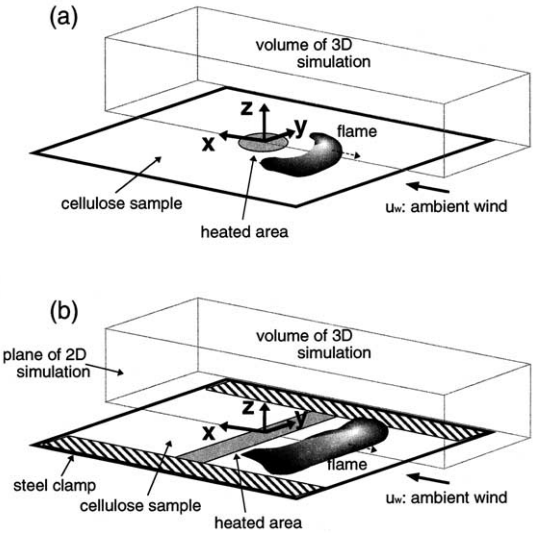

Fig. 1. Schematic illustration of the computational simulation domains. (a) spot ignition and (b) line ignition.

nal: all RITSI experiments were conducted in air and all flames were small and their color was mainly blue. Furthermore, all walls of the RITSI hardware were painted black to minimize reflection of emissions from the flame. Because these assumptions were used for both cases with and without the enclosure, the calculated enclosure effects should not be significantly affected.

A global, finite-rate, one-step gas phase reaction of fuel and oxygen is assumed. Reaction parameters are identical to those from past studies [7, 8, 10, 11, 15]. The stoichiometric constant, $\nu_g = 3.213$, is slightly modified from its previous value of 3.57 because the molecular weight of each species is included, rather than assuming that of air as in our previous studies. The gas phase reaction parameters used in the present study are summarized in Table 2. Transport properties are estimated from kinetic theory, unlike previous studies where it was assumed all gases had the same transport properties. The binary diffusion coefficient of each gas component is assumed to be that of the given species diffusing into nitrogen. Transport properties and molecular weights of the combustion products are assumed to be identical to those of nitrogen, a major gas component.

Configurations

Figure 1 shows the computational domains in the cases of (a) spot ignition and (b) line ignition. In the 3-D simulation, the following two configurations are of interest for (a) spot ignition: open, and tunnel-like enclosure (i.e., enclosed) cases, whereas only the enclosed case was studied for (b) line ignition. In the 2-D simulation (line shape flame), both open and enclosed (with a top boundary) cases are considered. Note in the case of enclosed line ignition (Figure 1b, 3-D), the sample paper is held by a steel clamp at the edges. Properties of the clamp are identical to those used in the RITSI experiment (for details, see Ref. 15). External flow is imposed from right to left with a spatially uniform velocity, u_w, at the entrance of the chamber. The ignition center on the sample paper is located at 8.6 cm downstream from the entrance in the 3-D simulation, and at 6.0 cm downstream in the 2-D case.

Initial and Boundary Conditions

The ignition is induced by a radiant thermal flux, identical to that employed in our past studies [7, 8, 10, 11, 15]. Following an initial time interval to establish the steady flow field, the radiant flux is turned on and increases with time following an experimentally determined profile. The flux is turned off after 3.5 s from the onset of radiation. The incident radiant flux distribution is approximated to be Gaussian with a peak of 70 kW/m^2 and half-widths of 0.25 cm and 0.75 cm in the line and spot ignition cases, respectively.

At the solid-gas boundary, the boundary conditions of quantities are identical to those used in our past studies [7, 8, 10, 11, 15]. They are:

$$u_x = u_y = 0.0, \qquad u_z = \dot{m}/\rho_g,$$

$T_g = T_S$, and $\dot{m}Y_{g,i} - (\rho_g D \nabla Y_{g,i}|_{on\ surface}) = \dot{m}_i$.

where, $\dot{m}_{ox} = -(\nu_{O2,ox}\dot{\omega}_{ox} + \nu_{O2,char}\dot{\omega}_{char}) \cdot \delta$,

$$\dot{m}_f = (\nu_{f,p}\dot{\omega}_p + \nu_{f,ox}\dot{\omega}_{ox} + \nu_{f,char}\dot{\omega}_{char}) \cdot \delta.$$

At the enclosure wall (non-slip surface), the temperature is fixed at room temperature, and the normal gradient of the species concentrations is set to zero. For the open case without enclosure, zero gradient conditions are used for the farfield boundary values of temperature and species concentration which decay exponentially with distance from the flame. This is not appropriate for the velocity field which decays quadratically [7]. Instead, boundary conditions were obtained from an analytically determined velocity potential using a Green's function including heat and mass addition to the computational domain [7, 11]. At the inlet boundary, the temperature and species concentrations are ambient, whereas zero gradient conditions are applied at the outlet boundary.

The selection of appropriate velocity boundary conditions at the inlet is a difficult task for the case with an enclosure. The addition of heat and mass from ignition and flame growth generates an expansion that modifies the inlet flow. Because the heat release and mass addition of the products from solid pyrolysis changes with time, the inlet flow boundary condition should be updated at each time step. Without the enclosure, the upstream and far field velocity field can be obtained from an analytical solution of the potential equation [7, 8, 10, 11, 15]. However, the same approach cannot be used for the case with an enclosure because the appropriate potential flow cannot be calculated for the enclosure geometry. In the experiment, a small fan was used at the outlet to generate specified flow conditions. The fan was calibrated without any addition of heat and mass to the flow field in normal gravity. Therefore, the effects of the heat and mass addition on fan characteristics in microgravity are not known. To determine the magnitude of this effect, two extreme conditions are considered in the present study: all expansion effects are assumed to go either downstream or upstream. The former means that the inlet flow condition is fixed during the calculation and the latter means that the outlet flow condition is fixed. The boundary condition appropriate to the actual experiment should be somewhere in between these two cases.

For the outflow-fixed boundary condition, the velocity profile at the downstream boundary can vary, but the average velocity is kept constant. Under this condition, the expansion effects will only appear upstream, and the reduction of the incoming flow because of expansion effects will be over-estimated. Note that the flow profile at the upstream boundary for the case with an enclosure is uniform. In the rest of the paper, we simply refer to these two extreme boundary conditions as 'inflow-fixed' and 'outflow-fixed,' respectively.

NUMERICAL MODEL

The numerical analyses were performed using a modified version of the Fire Dynamics Simulator (FDS) [17, 18] developed at NIST. The above governing equations of the gas and solid phase are written in finite difference form and spatial derivatives are calculated to second order accuracy using a scheme which is a weighted combination of central and upwind differences with the weighting factor controlled by the local Courant number. Gas phase variables are updated in time by an explicit, second order accurate predictor-corrector scheme. Those of the solid phase are updated by a first order, explicit Euler method. The divergence condition is enforced by solving a Poisson equation for the pressure using a direct Poisson solver [19]. The each time step is optimized in each time step to satisfy the Courant-Friedrichs-Lewy (CFL) condition. To account for numerical stiffness in the solid phase reactions, the time step used in the solid phase routine is reduced by a factor of 100 from that of the gas phase. Though FDS can be run either as a direct numerical simulation (DNS) or as a large eddy simulation (LES). All calculations in the present study were performed with the DNS mode.

Numerical grid cells in the computational domain are rectangular and cell faces are perpendicular to the x, y, and z-axes (see Figure 1). A staggered grid is employed; scalar quantities are evaluated at cell center and velocity compo-

nents are evaluated at cell faces. A uniform numerical grid is used in two dimensional simulations, while a non-uniform, rectilinear grid is used in the three dimensional simulations (in the x- and z-direction). Cell sizes in the two-dimensional simulations range between 0.75 mm to 0.83 mm. Minimum cell sizes in the three dimensional simulations are 0.66 mm and 0.5 mm in the x- and z-directions, respectively, and stretched up to 2 mm in the far-field. Various grid resolutions were tested before present study and ensure the results shown in the present study are not significantly affected by the mesh size. A more detailed discussion about the characteristic length scales of this problem is provided in Appendix. The two dimensional computational domain is 12.0 cm $\times$ 6.0 cm, while the three dimensional domain is 16.5 cm $\times$ 5.95 cm $\times$ 6.0 cm. The corresponding grid dimensions are 150 $\times$ 80 (12,000 grids) for the two dimensional and 145 $\times$ 70 $\times$ 40 (406,000 grids) for the three dimensional simulation. The time to complete a typical three-dimensional calculation is approximately 20 h of CPU time per second simulated time on current generation workstations or personal computers. All calculations are conducted with 35% oxygen concentration incoming flow.

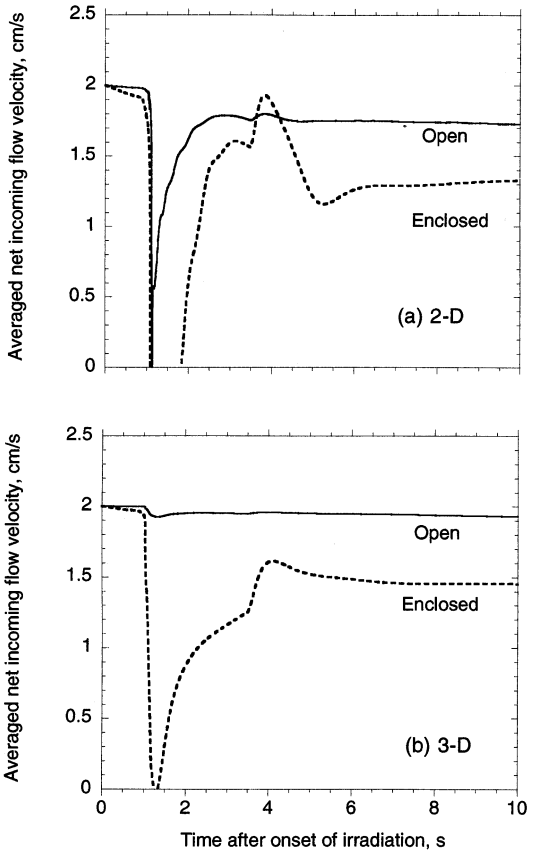

Fig. 2. Effects of the confinement on time-histories of the average net incoming flow velocity in (a) two dimensional configuration and (b) three dimensional configuration. Enclosed case with the outflow-fixed boundary conditions. Imposed flow velocity, u_w, is 2 cm/s.

RESULTS AND DISCUSSION

Time-Histories of Average Net Incoming Flow

First, expansion effects on the inlet flow velocity are evaluated with and without the enclosure both in 2-D and 3-D configurations. Figure 2 shows the time histories of the average net incoming flow velocity for cases where the outflow velocity is fixed at 2 cm/s for the case with the enclosure. In the 2-D configuration, ignition is initiated across the sample width and in 3-D at a small circular ignition point, as shown in Figure 1 (a). The abscissa indicates the elapsed time from the onset of the irradiation to the sample surface. The average incoming flow decreases abruptly at around 1 s, then slowly converges to a quasi-steady value. The abrupt change is because of the thermal expansion caused by the onset of ignition. The reduction is larger for the 2-D configuration than that in the 3-D configuration because of larger heat release for the former (line across the sample width) than the latter (small spot size). Also the 2-D thermal expansion can only propagate upstream with the enclosure using the fixed out flow boundary condition. Thus, flow reversal occurs in the 2-D configuration with the enclosure. Because the irradiation is turned off at 3.5 s, the incoming flow increases at around this time because of reduced thermal expansion. After about 4 s, another large reduction in the incoming flow velocity occurs, in particular, in the 2-D configuration with the enclosure. The reason for this will be discussed in the next section.

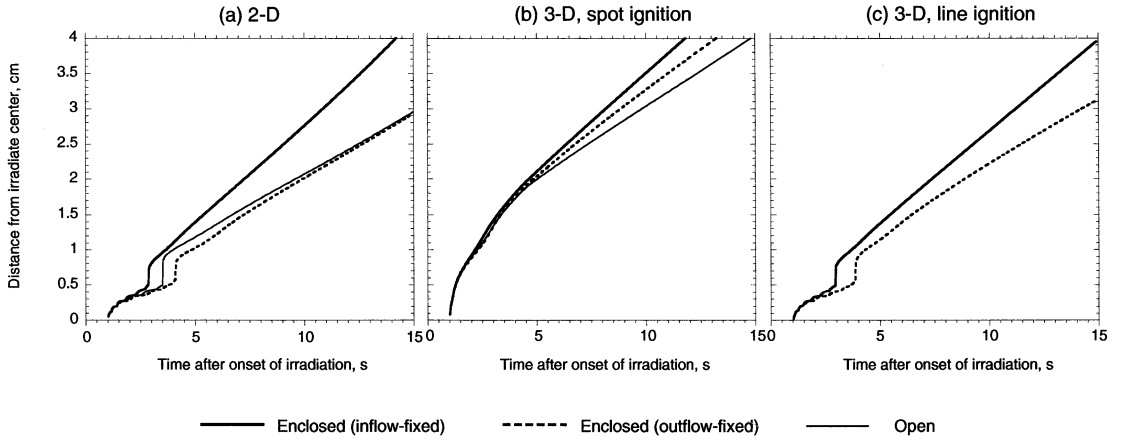

Fig. 3. Effects of the confinement on time-histories of the location of char front in (a) two dimensional configuration, (b) three dimensional configuration with spot ignition, (c) three dimensional configuration with line ignition with various imposed flow boundary conditions. Imposed flow velocity, u_w, is 2 cm/s.

Upstream Flame Spread

For the slow imposed flow velocities used in our previous studies [7, 8, 10, 11], it was observed that flame spread from a localized ignition occurred only in the upstream direction unless the ambient oxygen concentration is extremely high. Figure 3 shows time histories of the position of the char front along the upstream centerline for the various configurations including both inflow-fixed and outflow-fixed cases with the enclosure. The location of the char front is defined as the point on the sample where 10% of the mass is lost from its original value. Note that there is an abrupt jump in the location of the char front in the early stage only for cases with a line ignition, but little for the 3-D spot ignition case. This behavior will be explained in later. From the figure, the effects of enclosure are found to be minor in early stage (we call a transition stage), but clearly become significant later (growth stage). In the later stage, the char front location changes are nearly linear with time, indicating that the flame spread rate reaches a quasi-steady value. This is mainly because of two competing factors; the increase in convective oxygen supply because flame travels upstream where thinner boundary layer is formed (this makes the spread rate increase), and the decrease of the net incoming flow (this makes the spread rate decrease) when the flame becomes larger (more heat release and larger thermal expansion) in the chamber. Therefore, the quasi-steady spread rate is used as the upstream spread rate in this paper.

The abrupt jump noted above is explained by Fig. 4 showing a typical time-sequence of (a) the reaction zone in the gas phase, and (b) distributions of the solid density in the sample for the case with a line ignition. At the onset of gas phase ignition, the flame expands significantly. In the transition stage from the ignition to flame spread, the flame gradually shrinks towards the sample surface. Eventually, the flame is anchored close to the sample surface and forms a slowly moving flame front. During this transition stage, the sample is heated by two heat sources—the external radiant flux and the flame. The former is mainly concentrated within 0.5 cm and the latter appears to be beyond 1 cm from the irradiated center. This is the reason why the density distribution shows two valleys. Because the char front is defined at points where the sample retains 90% of the initial density, the char front jumps from the first valley (external radiation) to the second (heat feedback from the flame) and the upstream jump of the char front, as seen in Fig. 3 with line ignition. If the time history of the flame front is plotted using the flame images shown in Fig. 4a, the flame initially moves rapidly towards the upstream, then backwards to the irradiated center, and then finally more slowly upstream. However, this abrupt jump of the char front and

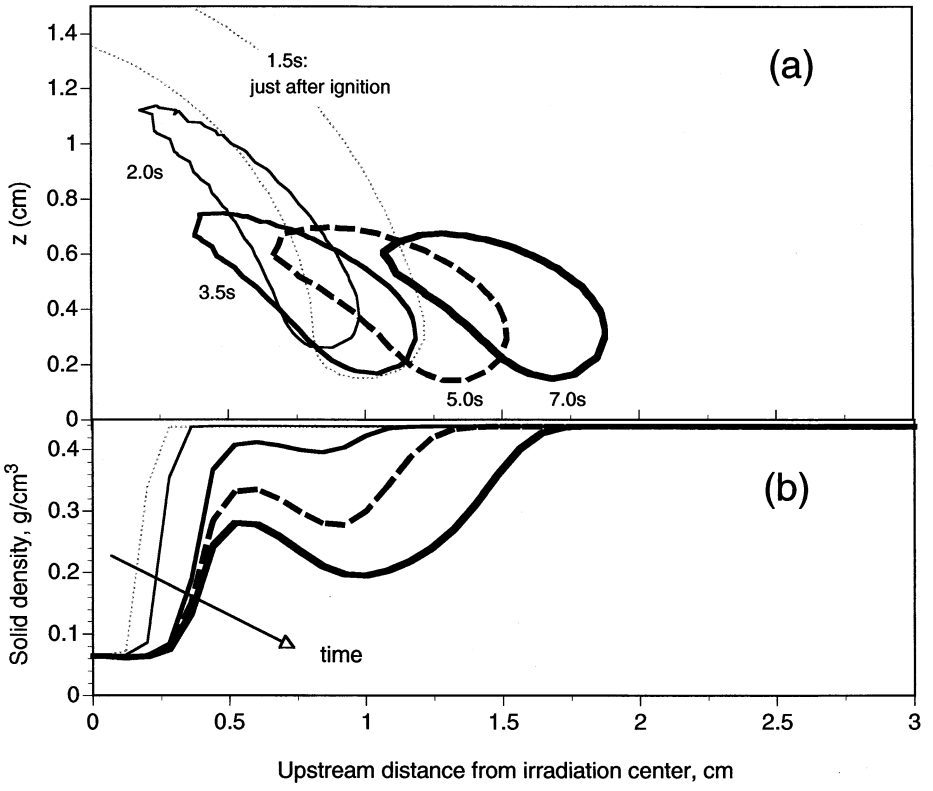

Fig. 4. Time-sequences of (a) flame image in gas phase and (b) distribution of the solid density in the two dimensional simulation. Flame is represented by the contour surface of the gas phase reaction rate of 1.0×10^{-4} g/cm^3 s. Imposed flow velocity, u_w, is 2 cm/s.

the back and forth movement of the flame front disappears as the imposed flow velocity increases. Because the flame expansion at the onset of a spot ignition is less than that at the onset of a line ignition, the abrupt jump of the char front cannot be seen with the spot ignition (see Fig. 3).

The flame anchoring process as discussed above starts around 4 s after irradiation (see Fig. 4a) and enhances the heat feed back rate to the sample surface. This increases the solid decomposition reaction rate below the anchoring point (see Fig. 4b), the mass addition to the gas phase, and subsequently the heat release. The increased heat release in turn reduces the net incoming flow velocity in the 2-D configuration with the enclosure, as seen in Fig. 2.

Spread Rate Versus Imposed Flow Velocity

Figure 5 shows the upstream centerline spread rate as a function of the imposed flow for the various configurations. The overall trend of increasing spread rate with u_w is found to be consistent with the previous studies [11] and experimental observations [1, 12, 20] regardless of the effects of the enclosure or the imposed boundary conditions. The enclosure effect is more significant at slower flow velocities near the quenching limit (~2 cm/s). It becomes less significant as the imposed flow velocity increases. The effect of the enclosure is more significant in 3-D than in 2-D. This implies that the lateral confinement enhances more oxygen flow into the flame. This enhances the flame significantly when oxygen is limited in cases of low imposed inlet flow velocities or low oxygen concentrations [5, 11, 15].

It is interesting that the flame spread rate for the inflow-fixed boundary condition is faster than that for the outflow-fixed boundary condition up to an imposed velocity of about 8 cm/s in the two dimensional configuration with and without the enclosure. For imposed flow veloc-

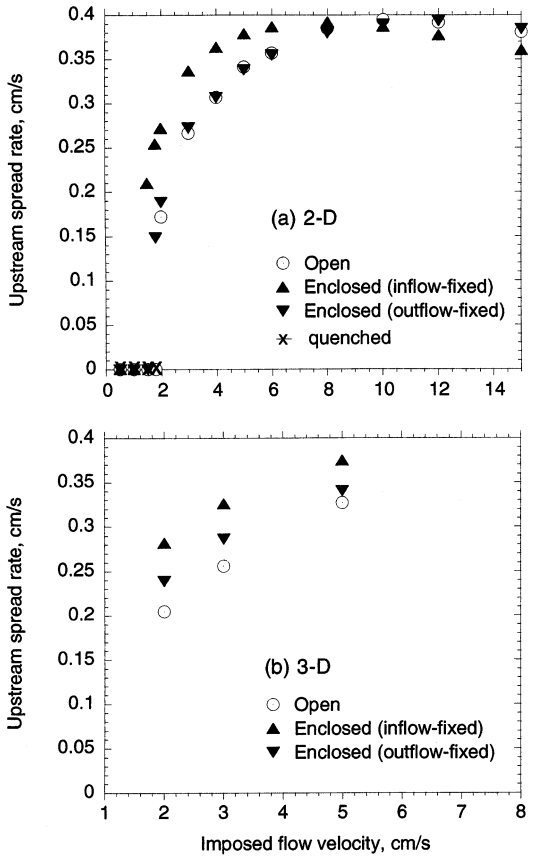

Fig. 5. Effects of the confinement on the relationship between upstream centerline spread rate and imposed flow velocity in (a) two dimensional configuration and (b) three dimensional configuration initiated by the spot ignition.

ities greater than 10 cm/s, the flame spread rate for the outflow-fixed boundary condition is faster than that for the inflow-fixed boundary condition. This happens for two reasons. First, the flame spread velocity decreases slightly with an increase in imposed flow velocity beyond a certain flow velocity due to cooling by the increased incoming flow. Second, the incoming flow velocity is reduced more for the outflow-fixed boundary condition. Therefore, the actual incoming flow velocity becomes less for the outflow-fixed case and it delays the reduction of flame spread rate by cooling. It is expected that a similar trend would be observed in 3-D if we calculate at higher imposed velocity than that shown in Fig. 5b.

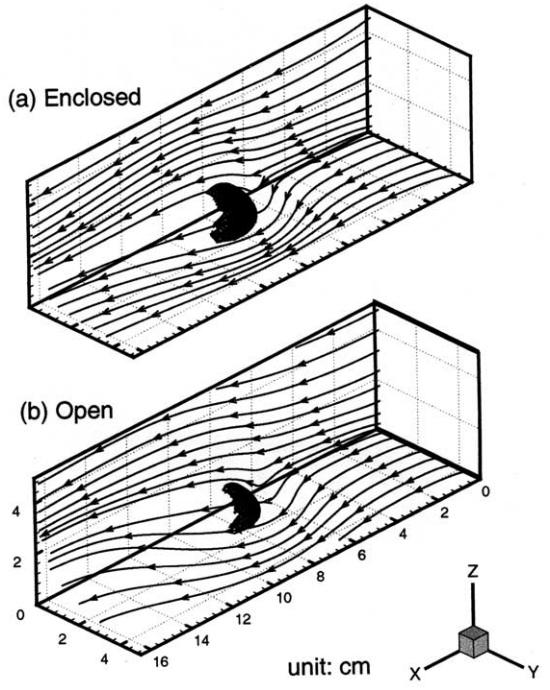

Fig. 6. Comparison of instantaneous flame image and 3-D flow streamlines; (a) with enclosure and (b) without enclosure. Shown streamlines are on y = 0 cm plane and slightly above from the paper surface. Flame is represented by the contour surface of gas phase reaction rate of 1.0×10^{-4} g/cm^3 s. Imposed flow velocity, u_w, is 2 cm/s.

Additional Oxygen Transport in Enclosure

In this section, the u_w = 2 cm/s simulation is discussed in detail because the enclosure effects are most pronounced (see Fig. 5). Figure 6 shows typical instantaneous streamlines and flame images for the enclosure case with the inflow-fixed boundary condition and the open case without the enclosure. With the enclosure, the confinement constricts the flow, especially near the wall, and the flow is accelerated. Such a flow modification changes the flame shape and oxygen transport processes. This is confirmed by the streamlines of oxygen mass flux shown in Fig. 7. Although only the results with the inflow-fixed boundary condition are shown in the figure, we confirmed that the same qualitative trend can be seen with the outflow-fixed boundary condition. Behind the flame, the oxygen mass flux streamlines are curved toward the flame for the enclosure case. This additional oxygen supply into the flame enhances the

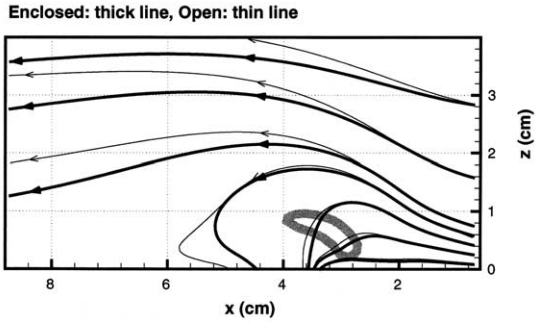

Fig. 7. Effects of the confinement on streamlines of oxygen in y = 0 cm plane. The enclosure case with inflow-fixed boundary condition. Figure is made when the flame front reaches at 3 cm upstream from ignition. Flame is represented by the contour surface of gas phase reaction rate of 1.0×10^{-4} g/cm^3 s. Imposed flow velocity, u_w, is 2 cm/s.

combustion there. Thus, the heat flux from the flame to the solid is slightly increased with the enclosure compared with that of the open case (nearly 5.4% increase for both inflow-fixed and outflow-fixed boundary conditions). As a result, the upstream spread rate for the case with the enclosure becomes faster than for the open cases when the oxygen supply to the flame controls the flame spread. This typically occurs for a low imposed flow velocity or a low oxygen concentration. The trend explained above is consistent with the results reported by Shih and Tien [12].

Three-Dimensional Configuration

Flame Spread Pattern

In the 3-D configuration with a spot ignition, we must also consider flame spread in the y-direction (transverse to flow direction) in addition to upstream. In this section, the multidirectional flame spread behavior for the case with and without the enclosure is examined under the condition of $u_w = 2$ cm/s. Figure 8 shows typical enclosure effects on time histories of the location of the char front of the sample for inflow-fixed boundary condition. The fan angle of the char growth pattern depends strongly on the presence or absence of the enclosure. The enclosure enhances significantly transverse flame spread in the y-direction and creates the wider fan angle of the char growth pattern. This trend is consistent with the experimentally observed

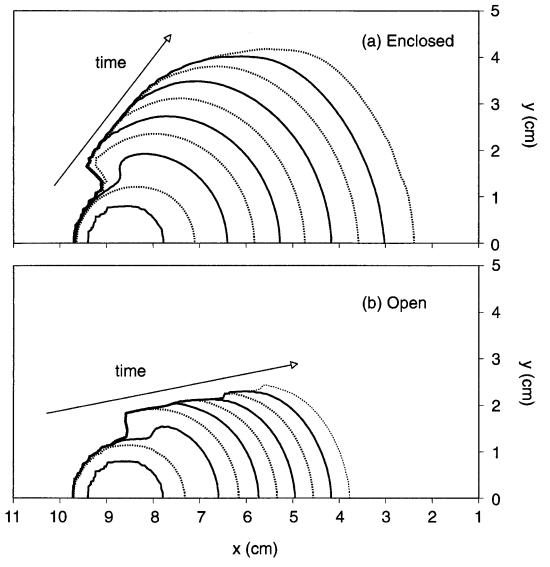

Fig. 8. Effects of the confinement on the char growth pattern from spot ignition at 2 s interval from the onset of ignition. The enclosure case with inflow-fixed boundary condition. Imposed flow velocity, u_w, is 2 cm/s.

results that show the fan angle increases with the increase in the imposed flow velocity [14]. It is expected that the enhanced flame spread in the transverse direction would be caused by the increased oxygen transport from the outer layer to the flame as observed in our previous studies [11, 15].

Figure 9 shows the relationship between the fan angle of the char growth pattern and the upstream centerline spread rate for the cases

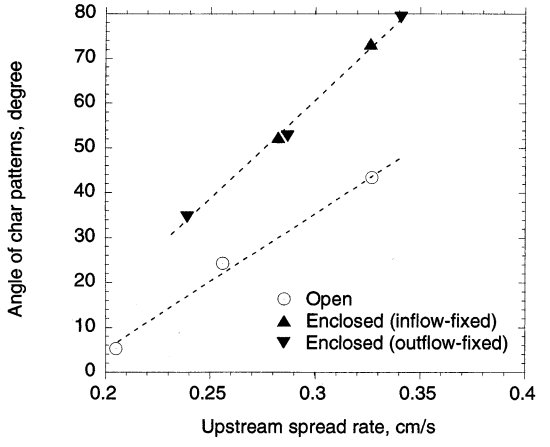

Fig. 9. Relationship between the fan angle of the char growth pattern and upstream centerline spread rate.

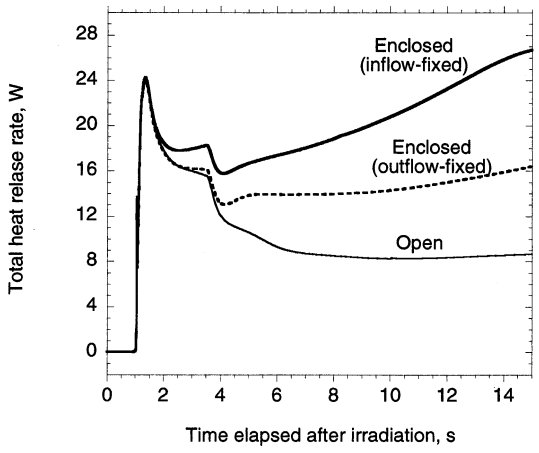

Fig. 10. The effects of the confinement on total heat release rate. Imposed flow velocity, u_w, is 2 cm/s.

with and without the enclosure at various imposed flow velocities (u_w = 2, 3, 5 cm/s). The figure indicates a linear relationship between the two quantities and the slope is steeper for the enclosed case. This trend is caused by higher acceleration of the flow between the flame and enclosure walls as discussed above. Note that the slope does not significantly depend on the flow boundary condition for the enclosure case. Because the degree of the acceleration of the flow between the flame and the enclosure walls depends on both the size of the flame and the enclosure dimension, the slope depends on the experimental configuration. This indicates that the upstream spread rate cannot describe the multi-directional flame spread behavior in the three dimensional configuration without including the enclosure effect.

Heat Release Rate

In Fig. 10, time histories of the total heat release rate are plotted during the flame growth period for the three cases at u_w = 2 cm/s. The figure clearly shows that total heat release rate is significantly higher for the enclosed flow regardless of the flow boundary conditions than that for the open case. With the inflow-fixed boundary condition, the heat release rate is nearly twice as large for the enclosed flow. Although quantitative effects of an enclosure on fire growth depend on the size of the enclosure and the amount of heat release [13], this result indicates that such effects should be included in flame spread predictions to make certain the spacecraft fire hazard is not underestimated. It also implies that measured flame spread rates are to some extent dependent on the apparatus configuration, which is a disturbing feature of microgravity experiments.

Line Ignition

Clearly, the enclosure plays a significant role on modifying the oxygen transport to the flame because of the flow acceleration caused by the confinement. This raises a question about the validity of the 2-D flame growth assumption used in our RITSI experiment. In the experiment, the 2-D line ignition was generated by a heated wire across the sample width. The sample was mounted on a metal sample holder that was attached to the enclosure walls. There was a narrow metal holder between the end of the sample and the walls. To examine the validity of our 2-D flame growth assumption, a 3-D calculation was performed with a line ignition.

The upstream centerline spread rate from the line ignition is compared for both 2-D and 3-D calculations in Table 3. The spread rate initiated from the spot ignition is also shown in the table for comparison. The spread rate induced by the line ignition with the 3-D calculation is found to be slightly slower than that with the 2-D calculation. The trend is opposite from one observed in our previous study without any enclosure, where the spread rate in the 3-D line ignition

TABLE 3

Comparisons of the Centerline Upstream Flame Spread Rate

	Three Dimensional (line ignition)	Two Dimensional	Three Dimensional (spot ignition)
inflow-fixed (enclosed)	0.270 cm/s	0.273 cm/s	0.282 cm/s
outflow-fixed (enclosed)	0.174 cm/s	0.189 cm/s	0.239 cm/s

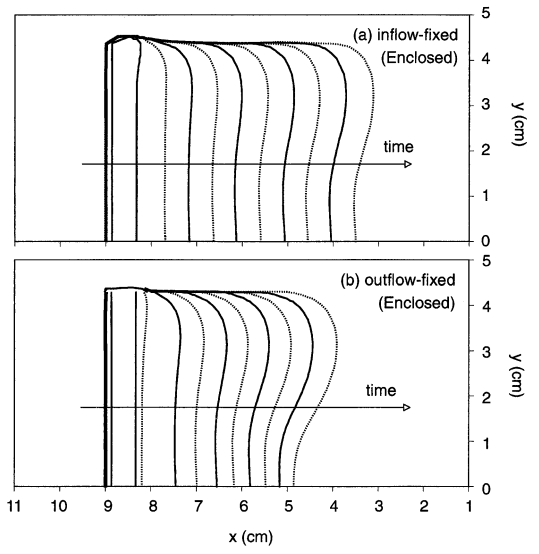

Fig. 11. Time-sequences of the shape of the char front initiated by line ignition; (a) inflow-fixed and (b) outflow-fixed boundary conditions with the enclosure. Imposed flow velocity, u_w, is 2 cm/s.

simulation is slightly faster than that in the 2-D simulation [15]. This is because of a combination of the confinement effect of the enclosure, the difference in the imposed far field boundary condition, and the heat loss to the side walls [5, 12, 15].

Validity of 2-D Assumption

Although the difference in upstream flame spread rate between the 2-D and 3-D line ignition simulations is relatively small, it is not clear that the upstream flame front remains two dimensional (line shape across the sample width) as the flame spreads upstream. Figure 11 shows the time histories of the char front in the enclosure. Note that the char front profile becomes more curved as the flame travels upstream. The distortion is quite significant with the outflow-fixed boundary condition. The fastest spread rate appears to be at 3 cm from the centerline (the edge of the sample is at 4.25 cm and the wall located at 5.1 cm). The distortion of the char front profile is due to the flow acceleration caused by the confinement that enhances the oxygen supply from the outer flow between the sample edges and the walls into the flame and by the heat loss to the sample holder. The degree of the distortion, however, depends on the imposed flow boundary condition. Because the imposed velocity, u_w = 2 cm/s, is in the oxygen supply controlled regime, the upstream flame spread rate strongly depends on incoming flow velocity. The outflow-fixed boundary condition reduces the incoming flow velocity due to the thermal expansion induced by the external radiation, ignition and the flame, as shown in Fig. 2. Therefore, actual incoming flow velocity with the outflow-fixed boundary condition is less than that with the inflow-fixed boundary condition. This implies the outflow-fixed case supplies less oxygen to flame than the inflow-fixed case. This is the reason why the distortion of the flame shape with the outflow-fixed boundary condition is more exaggerated than that with the inflow-fixed boundary condition. If the inlet flow velocity were decreased further, a similar behavior might be observed even under the inflow-fixed boundary condition.

The heat loss from the flame to the metal holder cannot be ignored. Without the heat loss, the spread rate becomes the fastest along edges of the sample instead of the char front patterns shown in Fig. 11 [21]. If the sample is extended to the chamber walls, the heat loss to the walls becomes more important [5]. To sum up, it appears that the 2-D approximation used in our RITSI hardware is not valid in the oxygen-controlled regime where the effects of the enclosure become significant.

CONCLUSION

Effects of the enclosure used in our early experiments on the transition from a localized ignition to subsequent upstream flame spread over a thermally thin cellulosic paper were studied by solving numerically the time-dependent low Mach number Navier-Stokes equations. The effects of the imposed flow boundary condition and geometrical configuration were examined for an imposed flow velocity of up to 15 cm/s in zero gravity. The conclusions are:

1. The effects of an enclosure on the transition from a localized ignition to subsequent flame growth are significant in the oxygen-controlled regime (low imposed flow velocities or low oxygen concentrations). The effects

become less important with an increase in imposed flow velocity. The enclosure constricts the flow field in the chamber and enhances oxygen transport to the flame front and also reduces inlet velocity due to thermal expansion induced by heat addition from external radiation, onset of ignition and subsequent flame growth. The enclosure effects are more pronounced for the 3-D configuration (spot ignition) than in the 2-D configuration because the enhanced oxygen transport to the flame is multi-dimensional.

2. The imposed flow boundary condition has significant effects on the enclosure flow simulation. Imposing correct flow boundary conditions including the effects of heat and mass addition from the flame is required to predict quantitatively flame growth behavior from ignition.
3. The flame spread pattern initiated by line ignition in a small chamber is a 3-D phenomenon in the oxygen-controlled regime.
4. A chamber must be large compared to the size of the flame if the enclosure effects are avoided. The enclosure effects increase significantly the total heat release rate during a flame growth period and they should be accounted to avoid underestimating fire hazard in a spacecraft. They also pose serious questions about the sensitivity of experimental results to apparatus dimensions.

This work is funded by the NASA Microgravity Science Program under the Interagency Agreement No. C-32-90-K under technical monitoring of Dr. Sandra L. Olson.

REFERENCES

1. Olson, S. L., Ferkul, P. V., and Tien, J. S., *Proc. of Combust. Inst*. 22:1213 (1988).
2. Frey, A. E. Jr., and Tien, J. S., *Combust. Flame* 36:263 (1979).
3. Bhattacharjee, S., and Altenkirch, R. A., *Proc. of Combust. Inst*. 23:1623 (1990).
4. Ferkul, P. V., and Tien, J. S., *Combust. Sci. Tech*. 99:345 (1994).
5. Shih, H. Y., and Tien, J. S., *Proc. of Combust. Inst*. 28:2777 (2000).
6. Di Blasi, C., *Combust. Flame* 97:225 (1994).
7. Nakabe, K., McGrattan, K. B., Kashiwagi, T., Baum, H. R., Yamashita, H., and Kushida, G., *Combust. Flame* 98:361 (1994).
8. McGrattan, K. B., Kashiwagi, T., and Baum, H. R., *Combust. Flame* 106:377 (1996).
9. Xi, J., and Weicheng, F., *Fire Safety J*. 24:279 (1995).
10. Kashiwagi, T., McGrattan, K. B., Olson, S. L., Fujita, O., Kikuchi, M., and Ito, K., *Proc. Combust. Inst*. 26:1345 (1996).
11. Mell, W. E., and Kashiwagi, T., *Proc. Combust. Inst*. 27:2635 (1998).
12. Shih, H. Y., and Tien, J. S., *Proceedings of Thirty-fifth Aerospace Sciences Meeting and Exhibit*, Reno, NV, AIAA 97-0236 (1997-1).
13. Baum, H. R., and Kashiwagi, T., presented at 2nd Joint Meeting of the U.S. Sections of the Combustion Institute, Oakland, CA (2001-3).
14. Olson, S. L., Kashiwagi, T., Fujita, O., Kikuchi, M., and Ito, K., *Combust. Flame* 125:852 (2001).
15. Mell, W. E., and Kashiwagi, T., *Proc. Combust. Inst*. 28:2785 (2000).
16. Kashiwagi, T., and Nambu, H., *Combust. Flame* 88:345 (1992).
17. McGrattan, K. B., Baum, H. R., Rehm, R. G., Hamins, A., and Forney, G. P., NISTIR-6467 (2000).
18. McGrattan, K. B., and Forney, G. P., NISTIR-6469 (2000).
19. Sweet, R. A., CRAY FISHPAK Ver. 1.1, Green Mountain Software (1990).
20. Olson, S. L., *Combust. Sci. Technol*. 76:233 (1991).
21. Mell, W. E., Olson, S. L., and Kashiwagi, T., *Proc. Combust. Inst*. 28:2843 (2000).

Received 17 October 2001; revised 8 April 2002; accepted 19 April 2002

APPENDIX

LENGTH SCALES

The spatial resolution required for the simulation cannot be decided solely on computational grounds. The problem has several fundamental length scales determined by both the geometry and the physical processes that must be evaluated. To understand these, it is necessary to consider the gas phase equations used to describe the scenario of interest in more detail. For this purpose, it is convenient to think of the energy and species equations in terms of two conserved scalar equations involving linear combinations of the reactants and the sensible enthalpy, together with an energy equation. Let the velocity be made non-dimensional with the nominal incoming velocity U, the spatial coordinates with respect to the half-width of the igniter spot 1, and let the density and diffusivity be normalized with respect to their cold ambi-

ent values. Then, the evolution equation for any conserved scalar F takes the form:

$$\rho\left(\frac{\partial F}{\partial t} + \vec{u}\cdot\nabla F\right) \equiv \frac{1}{Sc}\frac{1}{\mathrm{Re}}\nabla\cdot(\rho D\nabla F)$$

Here, ρ, u, and D are, respectively, the dimensionless density, velocity, and diffusivity in the gas. The Reynolds number Re and Schmidt number Sc are defined in terms of the above physical quantities and the ambient kinematic viscosity ν_∞ as follows:

$$\mathrm{Re} = \frac{U_{\infty l}}{\nu_\infty} \qquad Sc = \frac{\nu_\infty}{D_\infty}$$

Note that l is the smallest relevant geometric scale in the problem, and that the Schmidt number is of order unity. Thus, the smallest length scale L_m induced by the diffusion–convection balance is given by:

$$L_m = \frac{l}{\sqrt{\mathrm{Re}}}$$

Now consider the two limiting states of the problem under consideration. In the pre-ignition state, the reaction term in the energy equation is negligible and thus the enthalpy is also a conserved scalar. Thus, early in the simulation, L_m is the smallest length scale, controlling the rate at which energy from the heated spot is transferred to the gas. Once the fuel has begun to pyrolyze, it also controls the rate at which fuel is added to the gas. Once ignition has been achieved and vigorous burning is under way, the resulting diffusion flame, however complex its shape, is still described by the dynamics of the conserved scalars. Thus, even though the computations are not performed using these variables, they describe the minimum length scales that must be resolved to capture both the pre-ignition heating and the post-ignition flame spread. The role played by the reaction terms in the energy equation is to determine the time at which ignition occurs, describe the transition between the two states, and provide a description of the flame sheet structure as it evolves. The structure of a diffusion flame is NOT needed to calculate the local heat release rate in the gas (see Williams [1] for an asymptotic analysis of the diffusion flame). Indeed, Williams analysis assumes that the conserved scalar field is known in advance, and that the temperature varies little from that given by a flame sheet analysis. Only the reactant species profiles in the flame will be incorrect if the flame structure is not adequately resolved. In this respect, the calculations reported above are probably not accurate. However, the initiation of this transition is a locally spatially homogeneous phenomenon, which starts from a state determined by the diffusive–convective balance. Thus, if phenomena on the L_m scale can be resolved by the computations, then most of the combustion dynamics of interest will be captured. The calculations reported above involve velocities (which have significant enclosure effects) in the 2 to 5 cm/s range, and the spot Gaussian half-width is taken as 0.75 cm. The Reynolds number associated with the highest velocity is about 25, so that L_m = 0.15 cm. This means that there are 2 to 3 grid cells per unit minimum scale when the gas is cold. As it heats up, the minimum scale expands with the gas and the computations become even more accurate. These theoretical considerations are amply borne out by numerical experiments that indicate almost no grid dependence when cells of the size reported above are employed in the calculations.

REFERENCE

1. Williams, F. A. *Combustion Theory*. Benjamin/Cummings, Menlo Park, 1985, pp. 76–80.